PHYSICAL REVIEW B **99**, 214402 (2019)

Chemical disorder and spin-liquid-like magnetism in the van der Waals layered 5*d* transition metal halide $Os_{0.55}Cl_2$

Michael A. McGuire,[*] Qiang Zheng, Jiaqiang Yan, and Brian C. Sales
Materials Science and Technology Division, Oak Ridge National Laboratory, Oak Ridge, Tennessee 37831, USA

(Received 15 April 2019; published 3 June 2019)

Single crystals of the van der Waals layered 5*d* transition-metal compound $Os_{0.55}Cl_2$ were grown and characterized by x-ray diffraction, magnetization and heat-capacity measurements, and atomic resolution electron microscopy. The crystals are stable in air and easily cleaved. The structure is derived from the $CdCl_2$ structure type, with triangular layers of transition metal sites coordinated by edge-sharing octahedra of Cl and separated by a van der Waals gap. On average, only 55% of the metal sites are occupied by Os, and evidence for short- and long-ranged vacancy orders is observed by diffraction and real-space imaging. Magnetization data indicate magnetocrystalline anisotropy due to spin-orbit coupling, antiferromagnetic correlations, and no sign of magnetic order or spin freezing down to 0.4 K. Heat-capacity measurements in applied magnetic fields show only a broad, field-dependent anomaly. The magnetic susceptibility and heat capacity obey power laws at low temperature and low field with exponents close to 0.5. The power law behaviors of the low-temperature heat capacity and magnetic susceptibility suggest gapless magnetic fluctuations prevent spin freezing or ordering in $Os_{0.55}Cl_2$. Divergence of the magnetic Gruneisen parameter indicates nearness to a magnetic quantum critical point. Similarities to behaviors of spin-liquid materials are noted, and in total the results suggest $Os_{0.55}Cl_2$ may be an example of a quantum spin liquid in the limit of strong chemical disorder.

DOI: 10.1103/PhysRevB.99.214402

I. INTRODUCTION

An interesting intersection between crystal chemistry in low-dimensional structures and physics of magnetism with spin-orbit coupling is realized in 4*d* and 5*d* transition metal halides. Often such compounds form layered crystal structures with pseudo-2D magnetic sublattices [1], and interesting effects of metal-metal bonding and clustering are also known [2,3]. Much of the recent research in layered 3*d* transition metal halides is driven by interest in magnetic monolayer materials based on Cr and, more recently, V trihalides [4–10], while recent study of heavier transition metal halides is focused on the Kitaev spin liquid candidate $RuCl_3$, in which spin-orbit coupling plays a key role [11–14]. Since the spin-orbit coupling strength increases strongly with atomic number, this naturally motivates study of related Os compounds [15].

Although the study of osmium chlorides goes back many decades, there is still significant uncertainty about the structures, compositions, and magnetic behaviors of these materials. High-temperature and low-temperature polymorphs of $OsCl_4$ are reported in the literature [16,17]. Single-crystal diffraction revealed an orthorhombic structure for the high-temperature phase with infinite chains of edge-sharing $OsCl_6$ octahedra [18]. A cubic unit cell has been proposed for the low-temperature phase [19], but no further structural details have been published. Both polymorphs of $OsCl_4$ are paramagnetic with effective moments of 1.0–2.0 μ_B reported from measurements between room temperature and 77 K [16,17,20]. No lower temperature magnetic studies were found in the literature. Magnetic data down to liquid nitrogen temperature is reported for the trichloride, giving an effective moment of $1.2 - 1.6\,\mu_B$ [17]. Surprisingly, there have been few subsequent experimental studies of $OsCl_3$, likely due to difficulty in obtaining suitable samples of this phase [21], although recent calculations have predicted interesting magnetic and topological phenomena in $OsCl_3$ monolayers [15]. The formation of a nonstoichiometric chloride $OsCl_{3.5}$ has been reported and x-ray diffraction suggested similarities to the monoclinic $AlCl_3$-structure type adopted by Ru, Ir, and Rh trichlorides [21]. No magnetic data are available for this compound.

In our exploration of heavy transition metal halides and efforts to form $OsCl_3$ as an analog of the quantum spin-liquid compound α-$RuCl_3$, we found that sizable and cleavable crystals with the composition $OsCl_{3.6}$ could be obtained reproducibly. Here we report our technique developed for growing these crystals, a detailed study of the crystallography of this phase using powder and single-crystal x-ray diffraction and real-space imaging using scanning transmission electron microscopy (STEM) with atomic resolution, and the characterization of the magnetic behavior down to 0.4 K with heat capacity and magnetization measurements. We find that the average structure is best described by the rhombohedral $CdCl_2$ type with Os vacancies, so the composition is best written as $Os_{0.55}Cl_2$. Evidence of superlattices related to vacancy ordering are observed in x-ray diffraction and STEM. A 4 × 4 × 1 superstructure model describes the sharp diffraction peaks well, while diffuse peaks suggest an additional 3 × 3 modulation in the plane. Our results suggest that the material studied here, the low-temperature cubic form of $OsCl_4$ [19],

---

[*] McGuireMA@ornl.gov

and the previously reported $OsCl_{3.5}$ [21] are all instances of the same chemical phase.

Our magnetization measurements reveal single ion anisotropy from spin-orbit coupling, net antiferromagnetic correlations, and a paramagnetic effective moment near $2.2\,\mu_B$. Charge balance suggests an mixture of Os^{3+}, Os^{4+}, and vacancies on the triangular net, and the fitted effective moment indicates either enhancement of the expected moment for Os^{3+} or the presence of a moment on the nominally nonmagentic Os^{4+}. No magnetic ordering transition is detected in magnetization data, and the ac susceptibility shows no spin freezing down to 0.4 K. The only feature observed in the heat capacity is a broad and strongly field-dependent Schottky-like anomaly at low temperature. Both the magnetic heat capacity and low-field magnetic susceptibility follow power laws at low temperature, indicating gapless fluctuations and perhaps nearness to a quantum critical point. The observed behaviors associated with the strongly disordered triangular lattice of spin-orbit coupled moments in $Os_{0.55}Cl_2$ bear striking similarities to candidate quantum spin-liquid materials.

II. METHODS

The osmium chloride starting material was synthesized by reacting OsO_2 powder with the $AlCl_3$-KCl eutectic mixture at 400 °C in a sealed silica tube similar to Ref. [22]. The product of this reaction was thoroughly washed with water (see Supplemental Material [23]) and dried. About 1 g of the dried powder was loaded into a quartz tube of 16 mm inner diameter, 1.5 mm wall thickness, and about 10 cm length. After sealing under vacuum, the growth ampoule was put inside of a box furnace, heated to 800 °C in 5 h and held at this temperature for 8 h before cooling to 400 °C over six days.

Powder x-ray diffraction (PXRD) was performed using a PANalytical X'Pert Pro diffractometer with Cu-$K_{\alpha 1}$ radiation. Single-crystal diffraction was performed using a Bruker APEX diffractometer with Mo $K\alpha$ radiation on crystals mounted in paratone oil in a nitrogen cold stream at 175 K. Data were collected using SMART, integrated using SAINT-Plus, and the structures were solved and refined using ShelX. Quantitative elemental x-ray analysis was performed using a JEOL JXA-8200X electron microprobe analyzer instrument equipped with five crystal-focusing spectrometers for wavelength dispersive x-ray spectroscopy (WDS). For this study, a 15 kV accelerating voltage was utilized, with an electron beam current of 5 nA and probe diameter set to $10\,\mu$m. Elemental standards for Os and Cl were run using Os metal and NaCl before the quantitative analysis was run to improve the k-ratio accuracy and precision. Samples were prepared by exfoliating a fresh surface, carbon painting the samples directly to an Al stub, and then evaporating a 2–5 nm carbon layer on the sample surface to minimize charging effects during analysis. The composition was determined to be $Os_{0.55(2)}Cl_2$ using the average of 93 spots.

Several batches of $Os_{0.55}Cl_2$, including powders, small crystals and large crystals were chosen for the STEM measurements. These bulk samples were exfoliated by sonication in acetone. Drops of the resulting suspensions were deposited on lacey carbon grids and then dried in air. High-angle annular dark-field-STEM (HAADF-STEM) imaging was performed on an aberration-corrected Nion UltraSTEM-100 microscope operated at 60 kV with low current. The convergence semiangle of the incident probe was 30 mrad, and the HAADF images were collected with semiangle of $86-200$ mrad. Each HAADF image was collected by stacking 20 fast scanned images. Some HAADF images have been low-pass filtered in order to reduce random noise. The thickness for the HAADF imaging region was measured to be 6 nm from the corresponding zero-loss electron energy loss spectrum using the log-ratio method with the inelastic mean-free-path calculation as described in Refs. [24,25].

For magnetization measurements, crystals were mounted in plastic drinking straws with the field in the plane and out of the plane of the platelike crystals. Data was collected using a Quantum Design MPMSXL for temperatures between 300 and 2 K, and a Quantum Design MPMS3 with iQuantum He3 insert for temperatures between 1.8 and 0.4 K. Heat-capacity measurements were carried out between 10 and 0.37 K using the He3 option in a Quantum Design PPMS.

III. RESULTS AND DISCUSSION

The crystal growth described above produced $Os_{0.55}Cl_2$ crystals of a wide range of sizes as illustrated in Fig. 1(b). Smaller crystals tended to have a more regular faceted shape consistent with the underlying hexagonal symmetry, while the larger crystals formed as longer ribbonlike plates. All of the crystals were easily cleaved. Diffraction from cleaved surfaces showed sharp reflections associated with the layer stacking [Fig. 1(c)], but aggressively grinding the large ribbonlike crystals for PXRD produced severe strain and poor diffraction patterns. To obtain a useful pattern, the crystals were gently ground together with a fine powder of silicon. A Reitveld fit for the resulting pattern is shown in Fig. 1(d), using the $CdCl_2$-type structure shown in Fig. 1(a). This structure has a triangular layer of Os bonded to Cl anions with the resulting slabs separated from one another by a van der Waals gap. Refinement of the Os occupancy give a composition of $Os_{0.58}Cl_2$, similar to the composition of $Os_{0.55}Cl_2$ determined by WDS analysis.

High-quality single-crystal diffraction data could not be obtained from pieces taken from the large crystals due to damage and exfoliation that occurred during cutting; however, a unit cell and symmetry consistent with that determined from powder diffraction was apparent from the data. For structural refinements, single-crystal diffraction data was collected on smaller crystals [one of which is shown in Fig. 1(b)]. Analysis of the strong diffraction peaks revealed a structure like that shown in Fig. 1(a) and summarized in Table 2 with atomic positions listed in the Supplemental Material [23]. The refinement gives an occupancy of 0.55 for the Os site, consistent with the WDS and PXRD results. Based on weaker superlattice reflections, it was determined that the $CdCl_2$ structure shown in Fig. 1 represented only a subcell approximation, and that the true unit cell was larger due to vacancy ordering as discussed below.

Figure 2 shows precession images from single crystal x-ray diffraction data. The diffraction spots are labeled using the subcell structure described above and shown in Fig. 1(a). The subcell indexes the spots in the *0kl* plane well [Fig. 2(a)], but

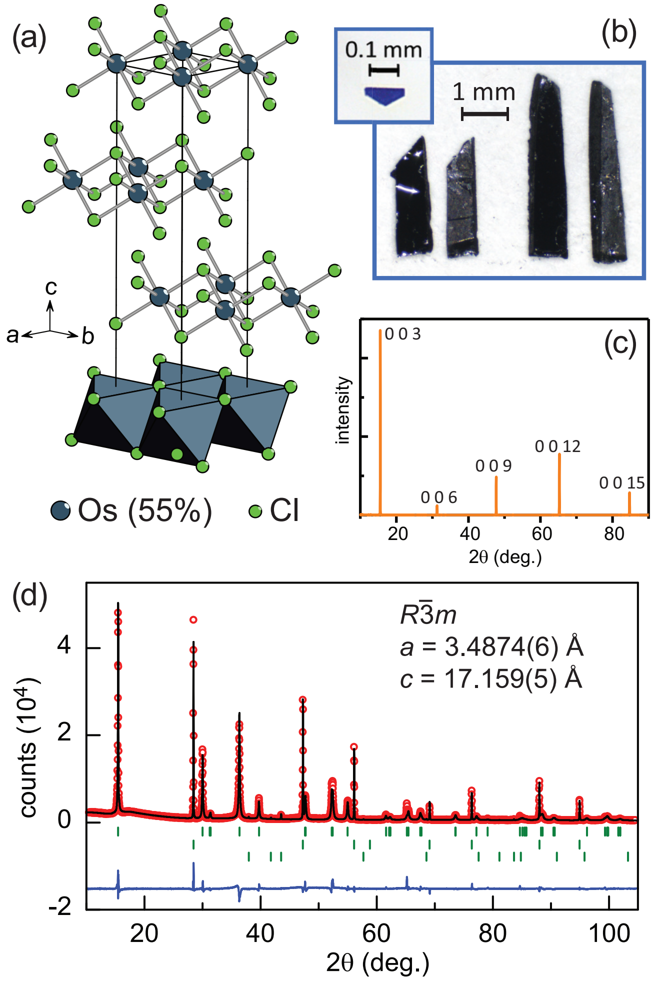

FIG. 1. (a) The $CdCl_2$-type average structure (subcell) of $Os_{0.55}Cl_2$. (b) A typical small crystal used for single crystal x-ray diffraction (upper left), and a two cleaved larger crystals used for other measurements. (c) X-ray diffraction data from a cleaved surface. (d) Rietveld fit of powder x-ray diffraction data from crystals ground with silicon powder. The upper, middle, and lower tick marks locate reflections from $CdCl_2$-type $Os_{0.55}Cl_2$ with the lattice parameters listed on the figure, silicon, and osmium from surface contamination, respectively.

additional reflections are seen in the *hk0* plane [Fig. 2(b)]. In the figures, circles are used to identify spots belonging to the subcell and the superlattice reflections are marked with squares and triangles. Sharp spots marked with squares indicate a 4×4 supercell in the plane. An additional set of spots, which are weaker and more diffuse, are marked with triangles and reveal an additional 3×3 modulation in the plane. Precession images of planes capturing diffraction from the superlattices only are shown in Figs. 2(c) and 2(d). All reflections from the 4×4 supercell are well defined and sharp, while those from the 3×3 modulation are diffuse along l, indicating that the ordering producing this diffraction is not coherent along the stacking direction. Interestingly, both of the superlattices evident from the diffraction from $Os_{0.55}Cl_2$ are distinct from the $\sqrt{2} \times \sqrt{2}$ vacancy ordering found in the closely related molybdenum compound $MoCl_4$ ($Mo_{0.5}Cl_2$) [26].

When the sharp superlattice reflections were included in the data analysis, a $4 \times 4 \times 1$ cell indexed the diffraction well and analysis of the intensities indicated a rhombohedral unit cell. The structure was refined in space group $R\bar{3}m$, the same space group as the subcell. The structure contains four unique Os positions within the layers and the superlattice arises from partial ordering of vacancies on these sites. The results of the structure refinement are summarized in Table I with atomic positions listed in the Supplemental Material [23]. The structure is shown in Fig. 2. In this superlattice model, the Os site occupancies vary from 0.29 to 0.62 and give an average occupation of 0.531(6) for the Os sublattice, similar to the refinement in the sublattice model [0.550(3)], powder diffraction [0.59(5)], and WDS analysis [0.55(2)]. Single-crystal diffraction results from a second crystal reported in the Supplemental Material [23] give an average Os occupancy of 0.550(3) and 0.552(6) using the subcell and supercell models, respectively. These results indicate the material is best described by the formula $Os_{0.55}Cl_2$.

With a structural model and composition established, this compound can be compared with previous reports of osmium chlorides. In Ref. [16], for the low-temperature form of $OsCl_4$, 11 measured diffraction angles were indexed to a cubic cell with $a = 9.95$ Å. Interestingly, the same lines can be indexed by a hexagonal cell with $a = 3.51$ Å and $c = 17.2$ Å, similar to the subcell in Table I. In fact, the primitive rhombohedral cell corresponding to the hexagonal supercell in Table I has $a = 9.88$ Å and $\alpha = 89.9^\circ$, metrically close to cubic and similar to the cell reported for low-temperature $OsCl_4$ [16].

The compound studied here is quite similar in composition to the material denoted $OsCl_{3.5}$ ($Os_{0.57}Cl_2$) in Ref. [21]. All but the weakest of the diffraction lines reported there are indexed by the subcell structure in Table I. This suggests that these may be the same compound. However, the existence of a compound with similar composition and a monoclinic structure related to the $AlCl_3$ type cannot be ruled out.

Finally, a comparison with the high-temperature orthorhombic form of $OsCl_4$ can be made. For orthorhombic $OsCl_4$, the authors reported clear orthorhombic symmetry from the diffraction pattern and crystals that break into fine fibers when handled [18], neither of which were seen in the present study. In addition, in the course of this work, it was noted that orthorhombic $OsCl_4$ could be converted into $Os_{0.55}Cl_2$ upon prolonged exposure to water [23]. Thus, it can be concluded that $Os_{0.55}Cl_2$ and orthorhombic $OsCl_4$ are indeed distinct phases; however, a close connection between the structures of these two phases can be drawn. Both structures are derived from the $CdCl_2$ structure type. In $Os_{0.55}Cl_2$ the Os vacancies are distributed in a way that appears to conserve the underlying three-fold symmetry of the structure. If instead, the vacancies are concentrated in chains along the [110] direction the structure could be broken up into 1-D chains of edge sharing $OsCl_6$ octahedra (for composition $Os_{0.5}Cl_2$), which is the structural motif of high-temperature, orthorhombic $OsCl_4$ [18].

As noted above, full single-crystal diffraction analysis of the large crystals was precluded by the damage induced by cutting the layered crystals to the size needed for the measurements. As a result, it was difficult to definitively confirm whether the superstructure described above was present in the

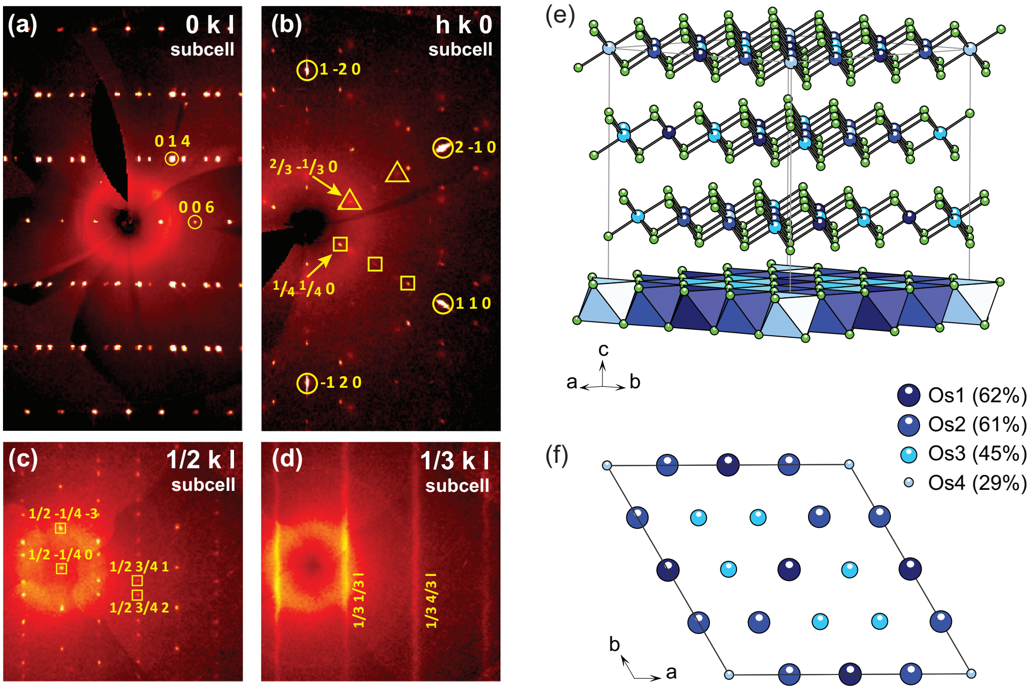

FIG. 2. Precession images constructed from single crystal x-ray diffraction data are shown in (a)–(d). All indices refer to the $CdCl_2$-type subcell (Fig. 1). (a) The $0kl$ plane showing no unindexed reflections between the l=integer planes. (b) The $hk0$ plane showing $\frac{h}{3}\,\frac{k}{3}$ superlattice reflections marked with triangles and $\frac{h}{4}\,\frac{k}{4}$ superlattice reflections marked with squares. (c) The $\frac{1}{2}kl$ plane showing sharp superlattice reflections. (d) The $\frac{1}{3}kl$ plane showing the diffuse nature of the $\frac{h}{3}\,\frac{k}{3}$ superlattice reflections along the layer stacking direction. (e) Superlattice model for Os-vacancy ordering in $Os_{0.55}Cl_2$ from single-crystal x-ray diffraction. (f) A single Os layer from the superstructure, with the size of the spheres representing the occupation of the four different Os sites in the model.

larger crystals. Diffuse reflections with 1/3-integer indices (relative to the subcell) were observed in the data, but spots expected from the 4 × 4 superlattice were not clearly seen. It is not clear if this indicates a difference between the details of the vacancy order in the large and small crystals or if it is related to damage and overall poor diffraction quality. Similarly, powder diffraction data from ground large crystals show only reflections indexed by the fully disordered subcell, suggesting that vacancy ordering is not present in the large crystals or that strain induced in the grinding process obscures the superstructure. To help resolve this and investigate the local structure further, real-space imaging with STEM was performed.

Results of the investigation of the local structure of a large $Os_{0.55}Cl_2$ crystal are summarized in Fig. 3. In the subcell structure viewed along the layer stacking direction, each atomic column identically involves Os and Cl atoms, therefore these atomic columns in HAADF-STEM images should show the same contrast. However, as a typical HAADF image displayed in Fig. 3(a), the intensities of these atomic columns reveal obvious variations. Since the HAADF image intensity is roughly proportional to Z^2 (Z is atomic number) and Os ($Z = 73$) is much heavier than Cl ($Z = 17$), this intensity fluctuation should be caused by Os vacancies, consistent with x-ray diffraction analysis. The superstructure reflections in its FFT pattern [the inset of Fig. 3(a)] indicate local ordering of the Os vacancies. This pattern shows sharp spots from the subcell and diffuse spots from a 3a × 3a supercell. This supercell is further confirmed by the real space HAADF images, as shown in Figs. 3(b) and 3(c), magnified from the regions marked in Fig. 3(a). The appearance of the 3a × 3a superlattice in certain regions of the HAADF image indicates some amount of coherence along the stacking direction does exist in those areas. However, this does not persist over large areas of the image, consistent with the overall poor coherence along the c axis indicated by x-ray diffraction [Fig. 2(d)]. In part of region 2, a superstructure with period 4a is also observed, confirming that, at least locally, superstructures similar to those identified by x-ray diffraction are also seem by STEM from the large $Os_{0.55}Cl_2$ crystals. Similar local

TABLE I. Results of single-crystal diffraction refinements for $Os_{0.55}Cl_2$ using data collected at 175 K including lattice parameters, Os site occupancies, resulting composition, and agreement indices. Both structure have space group $R\bar{3}m$.

	Subcell	Supercell
a (Å)	3.4851(9)	13.964(8)
c (Å)	17.114(6)	17.147(10)
Occ. - Os1	0.551(8)	0.62(2)
Occ. - Os2	–	0.61(1)
Occ. - Os3	–	0.45(1)
Occ. - Os4	–	0.29(1)
Composition	$Os_{0.55}Cl_2$	$Os_{0.53}Cl_2$
$R_1(I > 2\sigma)$	0.0269	0.0437
$wR_2(I > 2\sigma)$	0.0715	0.1707
R_1 (all data)	0.0269	0.0731
wR_2 (all data)	0.0715	0.2268

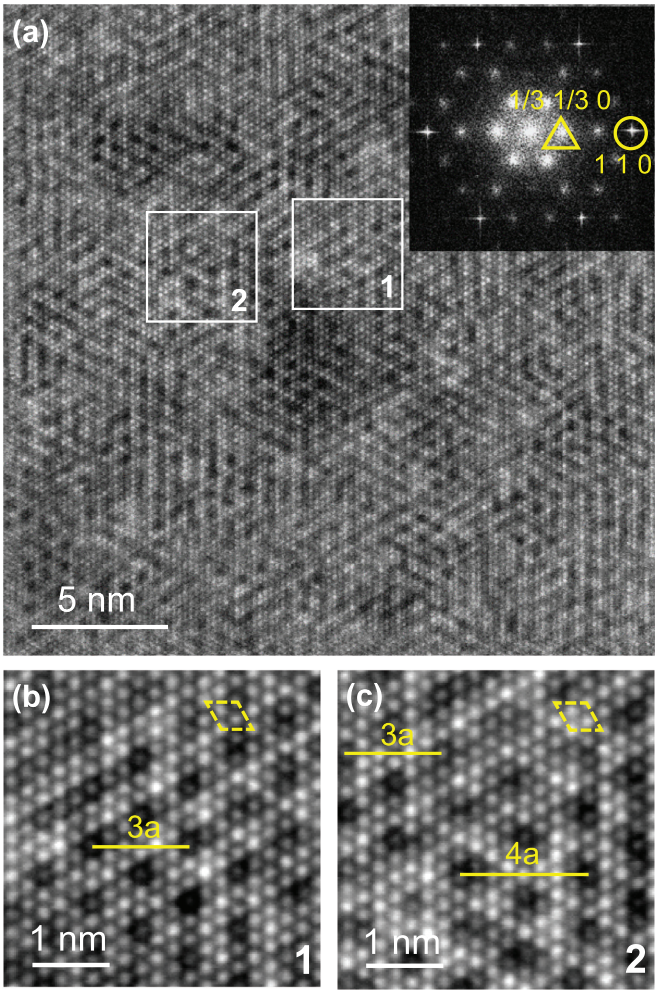

FIG. 3. HAADF-STEM for $Os_{0.55}Cl_2$ along [001] showing ordered Os vacancies. (a) A typical HAADF-STEM image and inset showing the fast-Fourier transform pattern with reflections indexed using the subcell structure. Low-pass filtered images of regions 1 and 2 in (a) are displayed in (b) and (c), respectively. The dashed line outlines the subcell, and the solid lines mark the vacancy ordering superstructure, with 3a and 4a periods apparent in regions 1 and 2, respectively.

structure features were also observed in smaller crystals and powder grains. This, along with the single-crystal diffraction data confirms that vacancy ordering on the Os sublattice occurs at some length scale in all of the $Os_{0.55}Cl_2$ crystals.

$Os_{0.55}Cl_2$ is electrically insulating. Gold contacts were sputtered onto the ends of a small crystal for resistance measurements. At room temperature, the resistance exceeded 50 MΩ.

Data from magnetization measurements on single crystals of $Os_{0.55}Cl_2$ are summarized in Fig. 4. The magnetic susceptibility (M/H) is anisotropic, as seen clearly in the temperature dependence between 2 and 300 K [Fig. 4(a)]. At 10 kOe, the anisotropy $(M/H)_{\perp c}/(M/H)_{\parallel c}$ increases from 1.2 at room temperature to a maximum of 2.7 at about 10 K. Nearly linear regions in the inverse susceptibility shown in the inset suggest Curie-Weiss-like behavior at the higher temperatures.

Charge balance would indicate 60% Os^{4+} and 40% Os^{3+} in $Os_{0.55}Cl_2$. The simplest spin-only picture with octahedral crystal field splitting gives $S = 1/2$ for Os^{3+} and $S = 1$ for Os^{4+}, corresponding to a Curie constant (C) of $0.75\,\mathrm{cm^3\,K\,mol\text{-}Os^{-1}}$. A single ion energy-level scheme incorporating spin-orbit coupling [27,28] predicts ground states of $J_{\mathrm{eff}} = 1/2$ for Os^{3+} ($5d^5$) and a $J = 0$ for Os^{4+} ($5d^4$), corresponding to $C = 0.15\,\mathrm{cm^3K\,mol\text{-}Os^{-1}}$. The data above 75 K were fit with a Curie-Weiss law plus a temperature independent contribution (χ_0). The fits are shown in the inset of Fig. 4(a). For $H \perp c$, the fit gives $\chi_0 = 2.36(4) \times 10^{-4}\,\mathrm{cm^3\,mol\text{-}Os^{-1}}$, $C = 0.268(1)\,\mathrm{cm^3\,K\,mol\text{-}Os^{-1}}$, and a Weiss temperature (θ) of 0.3(3) K. For $H \| c$, the fit gives $\chi_0 = 3.25(3) \times 10^{-4}\,\mathrm{cm^3\,mol\text{-}Os^{-1}}$, $C = 0.211(1)\,\mathrm{cm^3\,K\,mol\text{-}Os^{-1}}$, and $\theta = -53.8(5)$ K.

The fitted values of χ_0 are similar in the two orientations and are expected to include contributions from core diamagnetism of Os and Cl and van Vleck (VV) paramagnetism associated with Os^{4+} ions. The core diamagnetism is estimated to be $-1.15 \times 10^{-4}\,\mathrm{cm^3mol\text{-}Os^{-1}}$ [29]. This leaves a VV contribution of about $3.5\text{–}4.4 \times 10^{-4}\,\mathrm{cm^3mol\text{-}Os^{-1}}$, or $\chi_{VV} = 5.8 - 7.3 \times 10^{-4}\,\mathrm{cm^3[mol\text{-}Os^{4+}]^{-1}}$, since only the Os^{4+} ions are expected to contribute. This is similar to the values determined for isoelectronic ($5d^4$) Ir^{5+} in Ba_2YIrO_6 and related pentavalent iridates [30].

The Curie constants determined from the fits are, as expected, significantly suppressed from that calculated with spin-only values, but are still a bit larger than the value of $0.15\,\mathrm{cm^3K\,mol\text{-}Os^{-1}}$ predicted for the spin-orbit coupled scenario described above. If the Curie-Weiss magnetism arises solely from the 40% of the Os ion that are formally trivalent, then the average fitted value of $0.24\,\mathrm{cm^3\,K\,mol\text{-}Os^{-1}}$ corresponds to an effective moment of $2.2\,\mu_B$ per Os^{3+}. As noted, this is somewhat larger than the value of $1.73\,\mu_B$ expected for $J_{\mathrm{eff}} = 1/2$ (assuming $g = 2$). However, similar effective moment values of $2.1 - 2.7\,\mu_B$ have been reported for trivalent Ru ($4d^5$) in $RuCl_3$ [12,31–34]. An effective moment of $2.0\,\mu_B$ was reported for tetravalent Rh ($4d^5$) in Li_2RhO_3 [35]. Smaller values, closer to the expected $1.73\,\mu_B$, seem more common for tetravalent Ir ($5d^5$): $1.8\,\mu_B$ in Na_2IrO_3 [36], $1.6\,\mu_B$ in β-Li_2IrO_3 [37], and 1.7 and $1.4\,\mu_B$ in La_2MgIrO_6 and La_2ZnIrO_6, respectively [38]. While the observed effective moment in $Os_{0.55}Cl_2$ is consistent with trivalent Os with a slightly enhanced moment and tetravalent Os with $J_{\mathrm{eff}} = 0$, it is important to note that a scenario in which all the Os ions have some magnetic moment cannot be ruled out. Although the strong-spin-orbit scheme predicts the $5d^4$ state of Os^{4+} to be nonmagnetic, there are theories in which magnetism is expected for this electronic configuration [39,40].

In the presence of single ion anisotropy, the relationship between the magnetic exchange interactions and Weiss temperatures is not straightforward. Anisotropy produces an additional contribution to the effective Weiss temperatures. This is described in Ref. [41], where it is shown that even in the absence of exchange interactions, anisotropy produces a nonzero effective Weiss temperature. In the case of zero exchange interactions, the powder average of the Weiss temperatures ($\frac{1}{3}\theta_\parallel + \frac{2}{3}\theta_\perp$) is zero [41]. In $Os_{0.55}Cl_2$ this relationship is clearly violated, with a strongly negative $\theta_\parallel$ and nearly

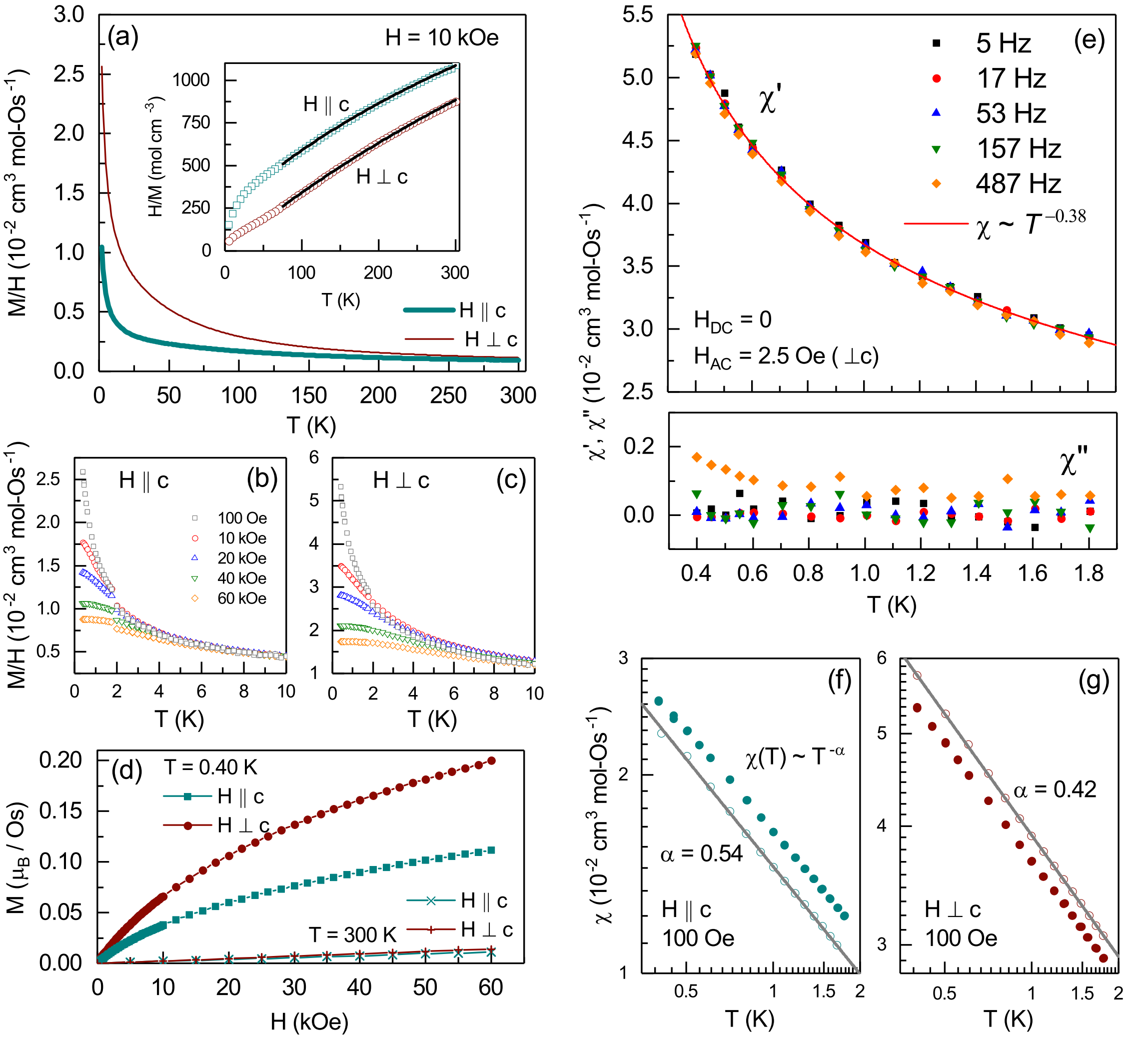

FIG. 4. Magnetic behavior of $Os_{0.55}Cl_2$ crystals. Magnetization data are shown for measurements along the layer stacking direction ($H \| c$) and in the plane of the layers ($H \perp c$) in (a)–(d). (a) Temperature dependence of the magnetic susceptibility (M/H) measured in a 10 kOe field. (b), (c) Low-temperature data measured at fields between 100 Oe and 60 kOe for the two orientations. (d) Isothermal magnetization curves measured at 0.4 and 300 K. (e) ac susceptibility showing the real (χ') and imaginary (χ'') component, and a power-law fit showing a $T^{-0.38}$ dependence. (f), (g) Log-log plots of low field susceptibility for two different crystals in both orientations, linear fits are shown and the extracted exponents are listed on the plots.

zero $\theta_\perp$, indicating net antiferromagnetic exchange. The powder average of the Weiss temperatures determined from the anisotropic measurements is -18 K. Powder averaging the temperature-dependent susceptibility data and then fitting over the same temperature range gives a Weiss temperature of -6.5 K. A density-functional-theory study of *monolayer* $OsCl_3$ with an ordered honeycomb arrangement of Os atom predicted ferromagnetic intralayer interactions [15], but this arrangement of Os atoms differs strongly from the structure of $Os_{0.55}Cl_2$ determined here.

The low-temperature magnetic behavior $Os_{0.55}Cl_2$ is shown in Figs. 4(b)–4(g). The dc magnetic susceptibility for the two orientations with applied fields ranging from 100 Oe to 60 kOe is shown in Figs. 4(b) and 4(c). The susceptibility increases monotonically upon cooling down to the lowest measurement temperature of 0.4 K. The small discontinuity near 1.8 K for H$\|$c is due to a mismatch between data sets collected in the ^{4}He and ^{3}He systems, probably related to a slight misalignment in mounting the crystal for the measurements. The data below 1.8 K were measured on warming after cooling from 5 K in zero field, and again after cooling in the applied field. No difference between zero-field-cooled and field-cooled data is observed. This is shown more clearly in the Supplemental Material [23].

Isothermal magnetization curves measured at the base temperature and 300 K are shown in Fig. 4(d). The absence of saturation at 0.4 K indicates significant antiferromagnetic interactions preventing alignment of the moments. Assuming 40% of the Os atoms have $J_{\mathrm{eff}} = 1/2$ a saturation moment of 0.4 μ_B would be expected. In the absence of antiferromagnetic interactions, saturation of moments with $g = 2$ and $J = 1/2$ would be expected with an applied field of only about 20 kOe. In addition, the remaining Os would generate a VV (linear) contribution to M vs H. The measured data reaches only 0.20 and 0.11 μ_B per Os for H in the plane and out of the plane, respectively.

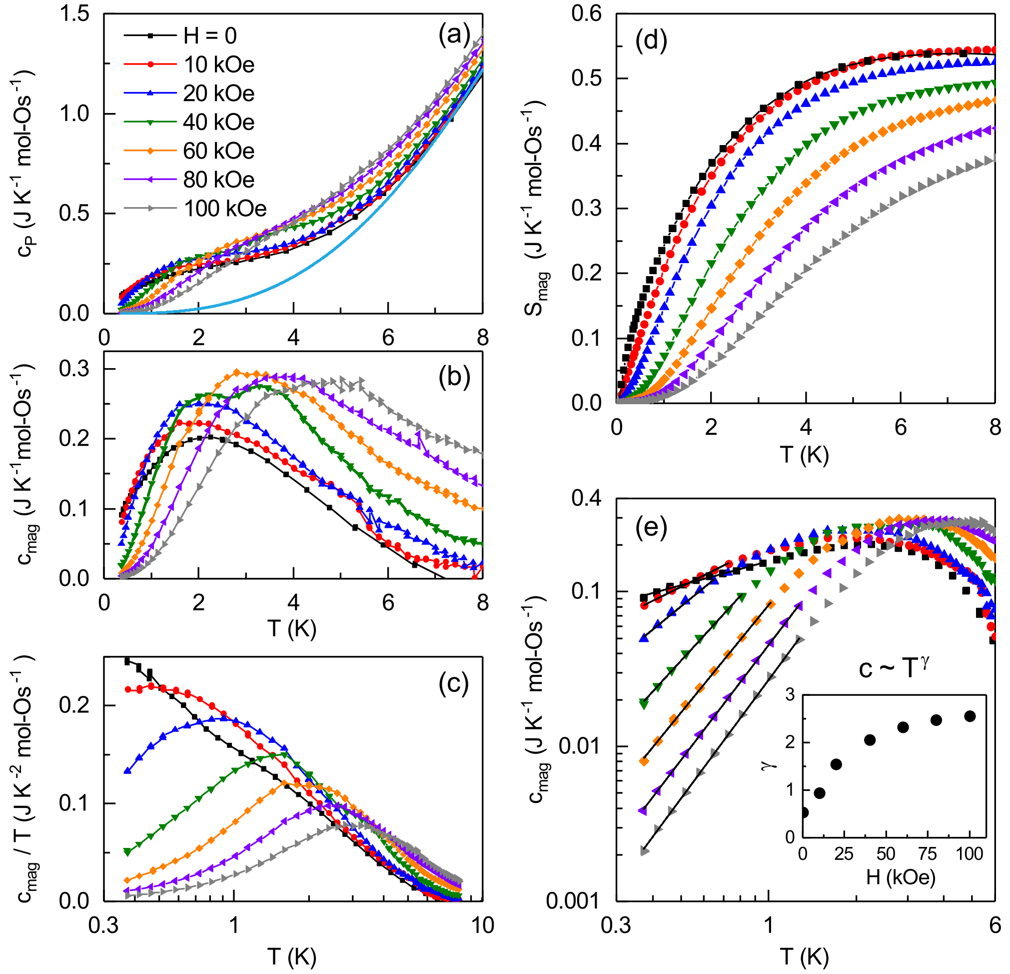

FIG. 5. Low-temperature heat capacity (c_P) of $\mathrm{Os_{0.55}Cl_2}$. (a) Measured heat capacity in magnetic fields applied out of the plane of the crystals ($H \| c$). The line shows an estimated phonon background determined as described in the text. (b), (c) Estimated magnetic contribution c_{mag} and c_{mag}/T. (d) Magnetic entropy estimated by integrating c_{mag}/T. (e) Log-log plot and power law fits for c_{mag}, with the field dependence of the fitted exponents shown in the inset.

Figure 4(e) shows the ac susceptibility measured in zero dc field between 0.4 and 1.8 K, with a 2.5 Oe ac field applied in the plane (⊥c). The real part (χ') mimics the low-field dc susceptibility, while the imaginary part (χ'') is generally featureless, showing only a small upturn at the lowest temperature at the highest frequency (487 Hz). No evidence of a glasslike transition is seen in this temperature range. Thus, the temperature and field dependence of the dc and ac magnetic susceptibility indicates the presence of antiferromagnetic interactions and the absence of long-range magnetic order or spin freezing down to 0.4 K. Thus, a lower bound of 16 can be placed on the frustration index $|\theta/T_N|$ of $\mathrm{Os_{0.55}Cl_2}$.

The susceptibility in low magnetic fields is observed to obey a power-law temperature dependence. This is demonstrated by the solid line fit to the χ' data in Fig. 4(e) and the log-log plots of the low field dc susceptibility in Figs. 4(f) and 4(g). The panels show data measured on two different crystals with H‖c and H ⊥ c, with power-law fits and fitted exponents labeled. For $\chi(T) \sim T^{-\alpha}$, the fits give $\alpha \approx 0.4$ for H ⊥ c and $\alpha \approx 0.5$ for H‖c. Interestingly, a power law with exponent close to 0.5 is also seen in the low-field heat capacity data described below.

Results of heat-capacity measurements are shown in Fig. 5. The data show no sharp anomalies that would indicate long-range magnetic order. Only a broad and field-dependent maximum is observed in the temperature range of 2–5 K. This anomaly is assumed to be of magnetic origin. Similar behavior was seen for $H \perp c$ shown in the Supplemental Material [23], but with smaller magnitude anomalies likely related to the smaller magnetic susceptibility for $H \perp c$ compared to $H \| c$ (Fig. 4). Since no suitable nonmagnetic reference material is available for determining a phonon background for this compound, data collected in zero field above 6 K were fit to a polynomial of the form $\beta T^3 + \delta T^5$ and used as a background. The magnetic heat capacity of $\mathrm{Os_{0.55}Cl_2}$ is estimated by subtracting this curve from the measured data [Fig. 5(b)].

The broad feature in the estimated magnetic heat capacity resembles a Schottky anomaly. However, its behavior deviates from the usual two level Schottky scenario in which the maximum value of the heat capacity is constant and the temperature at which the maximum occurs increases linearly with field [42]. In $Os_{0.55}Cl_2$ the position of the maximum is nearly independent of field up to 20 kOe, two separate maxima are seen at 40 kOe, and a single maximum that increase in temperature with increasing field is seen at higher fields. The peak value of the anomaly is also about an order of magnitude smaller than the expectation for a two-level Schottky anomaly ($3.65\,\mathrm{JK^{-1}mol^{-1}}$). As will be shown below, the temperature dependence below the peak temperature follows a power law rather than the exponential behavior expected for a Schottky (gapped) system.

The magnetic entropy was estimated by integrating c_{mag}/T and the results are shown in Fig. 5(d). To estimate the entropy, power laws (see below) were used to interpolate between the data and the origin, since in the lower magnetic fields c_{mag}/T is still relatively large at the lowest measurement temperatures [Fig. 5(c)]. The entropy determined at all fields with no interpolation is shown in the Supplemental Material, where the underestimation of the entropy in lower fields is apparent [23]. The maximum estimated magnetic entropy is $0.54\,\mathrm{JK^{-1}mol\text{-}Os^{-1}}$, about an order of magnitude smaller than $Rln(2)$. Broad heat-capacity features are often reported at low temperature in quantum spin-liquid candidates and frustrated magnetic systems, for example, $ZnCu_3(OH)_6Cl_2$ [43], $YbMgGaO_4$ [44,45], $Sc_2Ga_2CuO_7$ [46], $Ce_2Zr_2O_7$ [47], and $Ba_3CuSb_2O_9$ [48], and the behavior is sometimes considered intrinsic and sometimes attributed to crystallographic defects. In $Os_{0.55}Cl_2$ it may be that a low concentration of local structural arrangements associated with the distribution of trivalent, tetravalent, and vacant Os sites produce Schottky anomalies with more complicated energy-level schemes and degeneracies that are responsible for the observed behavior, although the power-law temperature dependence below the peak noted below may argue against this. Comparing the data in Figs. 5(a)–5(c) with the literature reveals behavior particularly similar to the quantum spin liquids $ZnCu_3(OH)_6Cl_2$ [43,49] and $YbMgGaO_4$ [44,45].

At the lowest temperatures, the heat capacity obeys a power law. This is shown in the log-log plots of c_{mag} vs T in Fig. 5(e). Linear fitting of the magnetic heat capacity was used to determine the exponent for a temperature dependence of the form T^{γ}. The fitted exponents are plotted as a function of applied field in the inset. In zero field $\gamma = 0.52$ is determined. This is similar to the exponent determined for the magnetization with H applied along the c axis [Fig. 4(f)]. The heat-capacity exponent increases with field and reaches 2.6 at 100 kOe. It appears that γ will approach a saturation value near 3.0, which is the exponent expected for antiferromagnetic magnons [42]. A similar field dependence has been reported for the magnetic heat capacity exponent in $YbMgGaO_4$ [44], where γ increased from 0.7 in zero field to 2.7 at 90 kOe. Smaller exponents, between 0.3 in zero field and 1.9 at 140 kOe, were reported for $Sc_2Ga_2CuO_7$ [46].

The power-law behavior of the low-temperature heat capacity and magnetic susceptibility suggests gapless magnetic fluctuations prevent spin freezing or ordering in $Os_{0.55}Cl_2$, and may indicate nearness to a magnetic quantum critical point. The magnetic Gruneisen parameter $\Gamma_{\mathrm{mag}} = -(dM/dT)/c$ compares the temperature derivative of the magnetization M to the heat capacity c, and is expected to diverge at such a critical point [50–52]. The observed exponents of $\alpha = 0.5$ for the magnetization and $\gamma = 0.5$ for the heat capacity at low temperature and zero field do indeed produce a divergence in Γ_{mag} as $T \rightarrow 0$, with an exponent close to 2. This divergence is suppressed when a field is applied, indicating that $Os_{0.55}Cl_2$ is near a quantum critical point in zero field, and the associated quantum fluctuations may be responsible for the spin liquid like behavior.

Neutron scattering studies of magnetic excitations and local probes of magnetism like muon spin rotation, especially if extended to even lower temperatures than the present study, would be desirable to further develop a more detailed understanding of the magnetic behavior in this material.

IV. SUMMARY AND CONCLUSIONS

The average structure of $Os_{0.55}Cl_2$ is of the layered $CdCl_2$ type with Os and vacancies distributed over the cation sites. Atomic resolution STEM finds vacancy ordering on various length scales in all of the samples imaged. X-ray diffraction from small single crystals reveals partial long-range vacancy order in three dimensions with a 4×4 superlattice within the layers, as well as diffuse reflections associated with 3×3 ordering that is incoherent along the stacking direction. Thus, the triangular cation lattice in $Os_{0.55}Cl_2$ contains significant disorder, with Os^{3+}, Os^{4+}, and vacancies partially ordered on short and long length scales and in 2 and 3 dimensions.

The magnetic susceptibility is anisotropic due to single ion anisotropy arising from spin-orbit coupling in the $5d$ metal Os. Data above about 75 K follow a Curie-Weiss law with a temperature-independent contribution consistent with VV paramagnetism of Os^{4+} ($5d^4$). The Curie constant or effective moment is larger than expected for 40% Os^{3+} with $J_{\mathrm{eff}} = 1/2$ and 60% Os^{4+} with $J_{\mathrm{eff}} = 0$, indicating either enhanced moment on the trivalent osmium or a nonzero moment associated with the $5d^4$ ions. The fitted Weiss temperatures indicate net antiferromagnetic interactions. The cleavable nature of this layered material suggests $Os_{0.55}Cl_2$ may provide a way to incorporate spin-orbit coupled magnetism into van der Waals heterostructures.

The geometrical frustration of the triangular lattice as well as the mixture of different electronic configurations and vacancies is expected to suppress long range antiferromagnetic order and would typically lead to a glassy magnetic state. Indeed, magnetic order above 0.4 K is not seen in magnetization and heat-capacity data. More interestingly, evidence of spin freezing is not seen in this data nor in ac susceptibility data, indicating $Os_{0.55}Cl_2$ is not a spin glass above 0.4 K. Nonsaturating isothermal magnetization curves at 0.4 K reveal antiferromagnetic correlations are still present at this temperature.

Only a relatively small and very broad anomaly is observed in the heat capacity of $Os_{0.55}Cl_2$ down to 0.37 K. The feature is broader than expected for a two-level Schottky anomaly, and displays a more complicated field dependence. While the origin of this anomaly is not clear, it is expected to be magnetic, and the temperature and field dependence of the heat capacity in $Os_{0.55}Cl_2$ are similar to behaviors observed in materials considered to be spin liquids or candidate spin liquids. At the lowest temperatures, below the peak in the anomaly, the magnetic heat capacity obeys a power-law temperature dependence [$c(T) \sim T^{\gamma}$] with an exponent near 0.5 in zero field and approaching $\gamma = 3$ expected for antiferromagnetic magnons at high fields.

The low field dc magnetic susceptibility and the ac susceptibility also obey power laws [$\chi(T) \sim T^{-\alpha}$] at low temperature with exponents of 0.4 to 0.5. The power-law behavior with exponent intermediate between noninteracting spins and isolated singlets suggests the magnetic order is suppressed by gapless fluctuations. The divergence of the magnetic Gruneisen parameter in zero magnetic field indicates that $Os_{0.55}Cl_2$ is near a quantum critical point, which may be the source of gapless magnetic fluctuations. While further studies are needed to fully understand the magnetic ground state of this material, the present results show strong indication of quantum magnetism in $Os_{0.55}Cl_2$, providing a system in which quantum criticality and spin-liquid behavior may be studied in the presence of strong spin-orbit coupling and chemical disorder.

ACKNOWLEDGMENTS

Research was supported by the U. S. Department of Energy, Office of Science, Basic Energy Sciences, Materials Sciences and Engineering Division under Contract No. DE-AC05-00OR22725. The scanning transmission electron microscopy in this work was conducted at the ORNL's Center for Nanophase Materials Sciences (CNMS), which is a DOE Office of Science User Facility. The authors thank A. Christianson, H. Zhou, and A. May for helpful discussions, R. Custelcean for use and assistance with the single-crystal x-ray diffractometer, and D. Leonard for performing the WDS microanalysis.

This paper has been co-authored by employees of UT-Battelle, LLC under Contract No. DE-AC05-00OR22725 with the U.S. Department of Energy. The United States Government retains and the publisher, by accepting the paper for publication, acknowledges that the United States Government retains a nonexclusive, paid-up, irrevocable, worldwide license to publish or reproduce the published form of this paper, or allow others to do so, for United States Government purposes. The Department of Energy will provide public access to these results of federally sponsored research in accordance with the DOE Public Access Plan.

---

[1] M. A. McGuire, Crystals **7**, 121 (2017).

[2] J. P. Sheckelton, K. W. Plumb, B. A. Trump, C. L. Broholm, and T. M. McQueen, Inorg. Chem. Front. **4**, 481 (2017).

[3] M. A. McGuire, J. Yan, P. Lampen-Kelley, A. F. May, V. R. Cooper, L. Lindsay, A. Puretzky, L. Liang, S. KC, E. Cakmak, S. Calder, and B. C. Sales, Phys. Rev. Mater. **1**, 064001 (2017).

[4] M. A. McGuire, H. Dixit, V. R. Cooper, and B. C. Sales, Chem. Mater. **27**, 612 (2015).

[5] W.-B. Zhang, Q. Qu, P. Zhu, and C.-H. Lam, J. Mater. Chem. C **3**, 12457 (2015).

[6] B. Huang, G. Clark, E. Navarro-Moratalla, D. R. Klein, R. Cheng, K. L. Seyler, D. Zhong, E. Schmidgall, M. A. McGuire, D. H. Cobden, W. Yao, D. Xiao, P. Jarillo-Herrero, and X. Xu, Nature **546**, 270 (2017).

[7] M. A. McGuire, G. Clark, K. Santosh, W. M. Chance, G. E. Jellison, Jr., V. R. Cooper, X. Xu, and B. C. Sales, Phys. Rev. Mater. **1**, 014001 (2017).

[8] S. Son, M. J. Coak, N. Lee, J. Kim, T. Y. Kim, H. Hamidov, H. Cho, C. Liu, D. M. Jarvis, P. A. C. Brown, J. H. Kim, C. H. Park, D. I. Khomskii, S. S. Saxena, and J. G. Park, Phys. Rev. B **99**, 041402(R) (2019).

[9] T. Kong, K. Stolze, E. I. Timmons, J. Tao, D. Ni, S. Guo, Z. Yang, R. Prozorov, and R. Cava, Adv. Mater. **31**, 1808074 (2019).

[10] S. Tian, J.-F. Zhang, C. Li, T. Ying, S. Li, X. Zhang, K. Liu, and H. Lei, J. Am. Chem. Soc. **141**, 5326 (2019).

[11] K. W. Plumb, J. P. Clancy, L. J. Sandilands, V. V. Shankar, Y. F. Hu, K. S. Burch, H.-Y. Kee, and Y.-J. Kim, Phys. Rev. B **90**, 041112(R) (2014).

[12] A. Banerjee, C. A. Bridges, J. Yan, A. A. Aczel, L. Li, M. B. Stone, G. E. Granroth, M. D. Lumsden, Y. Yiu, J. Knolle, S. Bhattacharjee, D. L. Kovrizhin, R. Moessner, D. A. Tennant, D. G. Mandrus, and S. E. Nagler, Nat. Mater. **15**, 733 (2016).

[13] P. Lampen-Kelley, A. Banerjee, A. A. Aczel, H. B. Cao, M. B. Stone, C. A. Bridges, J.-Q. Yan, S. E. Nagler, and D. Mandrus, Phys. Rev. Lett. **119**, 237203 (2017).

[14] M. Roslova, J. Hunger, G. Bastien, D. Pohl, H. M. Haghighi, A. U. Wolter, A. Isaeva, U. Schwarz, B. Rellinghaus, K. Nielsch *et al.*, Inorg. Chem. **58**, 6659 (2019).

[15] X.-L. Sheng and B. K. Nikolić, Phys. Rev. B **95**, 201402(R) (2017).

[16] P. Machmer, Z. Naturforsch. B **24**, 200 (1969).

[17] V. Belova and I. Semenov, Russ. J. Inorg. Chem. **16**, 1527 (1971).

[18] F. A. Cotton and C. E. Rice, Inorg. Chem. **16**, 1865 (1977).

[19] P. Machmer, Chem. Commun., 610a (1967).

[20] R. Colton and R. Farthing, Aust. J. Chem. **21**, 589 (1968).

[21] H. Schäfer and K.-H. Huneke, J. Less-Common Met. **12**, 331 (1967).

[22] J.-Q. Yan, B. Sales, M. Susner, and M. McGuire, Phys. Rev. Mater. **1**, 023402 (2017).

[23] See Supplemental Material at http://link.aps.org/supplemental/10.1103/PhysRevB.99.214402 for additional crystallographic data and results. .

[24] T. Malis, S. C. Cheng, and R. F. Egerton, Microsc. Res. Tech. **8**, 193 (1988).

[25] R. Egerton, *Electron Energy-Loss Spectroscopy in the Electron Microscope* (Springer, New York, 2011).

[26] M. A. McGuire and B. C. Sales, Phys. Rev. Mater. **2**, 074007 (2018).

[27] J. B. Goodenough, Phys. Rev. **171**, 466 (1968).

[28] B. J. Kim, H. Jin, S. J. Moon, J.-Y. Kim, B.-G. Park, C. S. Leem, J. Yu, T. W. Noh, C. Kim, S.-J. Oh, J.-H. Park, V. Durairaj, G. Cao, and E. Rotenberg, Phys. Rev. Lett. **101**, 076402 (2008).

[29] G. A. Bain and J. F. Berry, J. Chem. Educ. **85**, 532 (2008).

[30] T. Dey, A. Maljuk, D. V. Efremov, O. Kataeva, S. Gass, C. G. F. Blum, F. Steckel, D. Gruner, T. Ritschel, A. U. B. Wolter, J. Geck, C. Hess, K. Koepernik, J. van den Brink, S. Wurmehl, and B. Buchner, Phys. Rev. B **93**, 014434 (2016).

[31] J. M. Fletcher, W. E. Gardner, A. C. Fox, and G. Topping, J. Chem. Soc. A, 1038 (1967).

[32] J. M. Fletcher, W. E. Gardner, E. W. Hooper, K. R. Hyde, F. H. Moore, and J. L. Woodhead, Nature **199**, 1098 (1963).

[33] Y. Kobayashi, T. Okada, K. Asai, M. Katada, H. Sano, and F. Ambe, Inorg. Chem. **31**, 4570 (1992).

[34] M. Majumder, M. Schmidt, H. Rosner, A. A. Tsirlin, H. Yasuoka, and M. Baenitz, Phys. Rev. B **91**, 180401(R) (2015).

[35] Y. Luo, C. Cao, B. Si, Y. Li, J. Bao, H. Guo, X. Yang, C. Shen, C. Feng, J. Dai *et al.*, Phys. Rev. B **87**, 161121(R) (2013).

[36] Y. Singh and P. Gegenwart, Phys. Rev. B **82**, 064412 (2010).

[37] T. Takayama, A. Kato, R. Dinnebier, J. Nuss, H. Kono, L. S. I. Veiga, G. Fabbris, D. Haskel, and H. Takagi, Phys. Rev. Lett. **114**, 077202 (2015).

[38] G. Cao, A. Subedi, S. Calder, J.-Q. Yan, J. Yi, Z. Gai, L. Poudel, D. J. Singh, M. D. Lumsden, A. D. Christianson *et al.*, Phys. Rev. B **87**, 155136 (2013).

[39] G. Khaliullin, Phys. Rev. Lett. **111**, 197201 (2013).

[40] O. N. Meetei, W. S. Cole, M. Randeria, and N. Trivedi, Phys. Rev. B **91**, 054412 (2015).

[41] D. C. Johnston, Phys. Rev. B **95**, 094421 (2017).

[42] A. Tari, *The Specific Heat of Matter at Low Temperatures* (Imperial College Press and Distributed by World Scientific Publishing Co., 2003).

[43] J. S. Helton, K. Matan, M. P. Shores, E. A. Nytko, B. M. Bartlett, Y. Yoshida, Y. Takano, A. Suslov, Y. Qiu, J. H. Chung, D. G. Nocera, and Y. S. Lee, Phys. Rev. Lett. **98**, 107204 (2007).

[44] Y. Li, H. Liao, Z. Zhang, S. Li, F. Jin, L. Ling, L. Zhang, Y. Zou, L. Pi, Z. Yang *et al.*, Sci. Rep. **5**, 16419 (2015).

[45] J. A. Paddison, M. Daum, Z. Dun, G. Ehlers, Y. Liu, M. B. Stone, H. Zhou, and M. Mourigal, Nat. Phys. **13**, 117 (2017).

[46] R. Kumar, P. Khuntia, D. Sheptyakov, P. G. Freeman, H. M. Rønnow, B. Koteswararao, M. Baenitz, M. Jeong, and A. V. Mahajan, Phys. Rev. B **92**, 180411(R) (2015).

[47] B. Gao, T. Chen, D. W. Tam, C.-L. Huang, K. Sasmal, D. T. Adroja, F. Ye, H. Cao, G. Sala, M. B. Stone *et al.*, arXiv:1901.10092.

[48] H. D. Zhou, E. S. Choi, G. Li, L. Balicas, C. R. Wiebe, Y. Qiu, J. R. D. Copley, and J. S. Gardner, Phys. Rev. Lett. **106**, 147204 (2011).

[49] V. Shaginyan, M. Y. Amusia, J. Clark, G. Japaridze, A. Msezane, V. Stephanovich, Y. Leevik, and E. Kirichenko, arXiv:1806.11081.

[50] L. Zhu, M. Garst, A. Rosch, and Q. Si, Phys. Rev. Lett. **91**, 066404 (2003).

[51] P. Gegenwart, Y. Tokiwa, J. Donath, R. Küchler, C. Bergmann, H. Jeevan, E. Bauer, J. Sarrao, C. Geibel, and F. Steglich, J. Low Temp. Phys. **161**, 117 (2010).

[52] S. Manni, Y. Tokiwa, and P. Gegenwart, Phys. Rev. B **89**, 241102(R) (2014).